Nanoscale

RSC Publishing

PAPER

View Article Online
View Journal | View Issue

# Templated evaporative lithography for high throughput fabrication of nanopatterned films

Cite this: *Nanoscale*, 2013, **5**, 624

Talha A. Arshad and Roger T. Bonnecaze*

A new method for the fabrication of well-defined nanostructured deposits by evaporation-driven directed self-assembly of nanoparticles is proposed and studied theoretically. The technique comprises a film of suspended nanoparticles drying with its surface in contact with a topographically patterned membrane which promotes spatially varying evaporation, resulting in a patterned deposit. Membrane thickness and topography (in conjunction with the initial film height and concentration) allow the feature and residual layer dimensions to be controlled independently. Numerical solutions of equations governing the dynamics of the process show how the concentration profile evolves as a result of flow driven by heterogeneous evaporation. Analysis yields bounds on the dimensions of the dried deposit, and provides processing parameters to achieve specific patterns. It is estimated that films with 10 nm to 100 μm features can be fabricated with a drying time of 0.1–10 seconds per 10 μm of feature height above the residual layer (depending on membrane thickness), making this a promising method for high throughput pattern deposition.

Received 18th July 2012
Accepted 26th September 2012

DOI: 10.1039/c2nr31924a

**www.rsc.org/nanoscale**



## Introduction

The ability to fabricate 2-D arrays of nanostructures and nanostructured particulate films finds growing application in a wide variety of areas including plasmonic devices,[1,2] high-density data storage,[3,4] photonic crystals,[5,6] metallized ceramic layers,[7] microchip reactors,[8] biosensors[9,10] as well as masks in various forms of nanosphere lithography.[11,12] Typically, substrates with topographical[13,14] or chemical[15] patterns and/or external fields[16,17] have been employed to guide particles, polymers, cells and even DNA into a desired configuration. Such processes are often specific to a certain building block, limited to a few monolayers and necessitate multiple processing steps. Moreover, many traditional techniques are unsuited to metallic nanostructures.

Evaporation-induced convection and dewetting-mediated pattern formation in suspension droplets[18–22] and films[23–29] has been the subject of several studies, and the prospect of using such an approach to deposit patterned particulate and polymeric films is garnering increasing attention[30–45] due to the significant advantages it engenders.[12,46,47] It is low-cost, materials general and applicable to both mono- and multilayered assemblies.

Recently Harris *et al.*[44] performed experiments in which a suspension of particles was allowed to evaporate under a mask with periodic holes. Their results demonstrated that convection induced by heterogeneous evaporation results in particle migration towards regions of relatively fast evaporation, depositing either isolated features or a continuous film with raised features under the mask holes. Two challenges impede the application of such a method to commercial nanofabrication: prohibitively long drying times and imprecisely defined deposits. Pattern deposition took around two hours, and arbitrarily shaped mounds constituted the features.

To address these issues, we consider a film of suspended nanoparticles on a substrate with its top surface in contact with a solvent-permeable membrane of periodically varying thickness (Fig. 1). The membrane's topographic pattern imposes heterogeneity in evaporation rate, resulting in flow of the suspension from relatively slow to fast evaporation regions. As the liquid evaporates, the membrane descends at a speed corresponding to the average evaporation rate, thereby maintaining perfect wetting at the suspension–membrane interface. Particle distribution within the film evolves as they convect with the liquid and diffuse within it. This continues until any part of

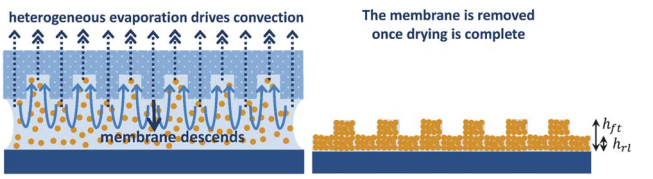


**Fig. 1** Schematic of templated evaporative lithography. Evaporation occurs more rapidly through the thinner regions of the solvent-permeable membrane, creating a convective flow which accumulates particles in those regions. The membrane descends at the average evaporation rate until it entraps close packed or a monolayer of particles against the substrate. A deposit with residual layer and feature heights $h_{rl}$ and $h_{ft}$ respectively is left behind once the entire suspension has dried.

*Department of Chemical Engineering, The University of Texas at Austin, Austin, TX 78712, USA. E-mail: rtb@che.utexas.edu*

the nanoparticulate film dries (*i.e.* the local particle volume fraction corresponds to random close packing), at which point the membrane ceases to descend but is left in place until the entire suspension has dried. Left behind is a deposit of particles with regions of varying height whose dimensions are determined by the pattern of the membrane mask and the properties of the nanoparticulate film. Deposits composed of metal nanoparticles can then be sintered to create a stable nanostructured film on the substrate.

The solvent-permeable polymeric membrane has a dramatic effect on drying time due to the presence of a steep solvent chemical potential gradient across a thin mask: the evaporation rate, when a sweep gas is blown across the unpatterned face of the membrane, is estimated to be $\sim 9\ \mu m\ s^{-1}$ for a 100 nm thick membrane,† compared to $\sim 10^{-2}\ \mu m\ s^{-1}$ reported by Harris *et al.*[44] *Via* template topography, this arrangement also imparts greater precision to the deposit than free surface evaporation and allows more flexibility in deposit shape than template-free techniques;[30–32] for the topography shown in Fig. 1, for example, rectangular stripes would be formed instead of mounds, and different template patterns can be used to define various 2D arrays.

A variety of methods exist for the fabrication of membranes with topographical features tens to hundreds of nanometers in size,[48–51] while the template can be positioned over the substrate down to a sub-20 nm resolution *via* the Moire alignment techniques used in imprint lithography.[52,53] We aim to understand the dynamics of the process to be able to tailor the system to deposit films of a desired pattern and assess its potential as a viable lithographic technique. Specifically, we investigate the following questions: can such an arrangement reduce drying time to a commercially acceptable level? What is the lower limit on drying time if effective particle segregation is to be maintained? How do parameters such as the membrane thickness and topography as well as the initial height and concentration of the suspension film affect deposit size and drying time? How does the fastest possible drying time vary with the desired feature size, and what is the optimal combination of parameters to achieve it?

In the following sections we first present the key equations describing the dynamics of the process and a numerical solution for the evolution of the flow and particulate concentration profiles. Next we develop analysis which yields bounds within which the dimensions of the deposit and drying time lie, providing a useful heuristic for the design of experiments targeting specific structures. These analytical expressions are used to investigate how experimental parameters govern deposit dimensions and drying time. Finally, performance limits in terms of shortest achievable drying time and minimum residual layer height for various feature sizes are estimated and compared with the experimental results of Harris *et al.*[44]

## Dynamics

The analysis is carried out in the context of a template with a step pattern as shown in Fig. 1, and symmetry in the problem is exploited to restrict the domain of interest to one half period

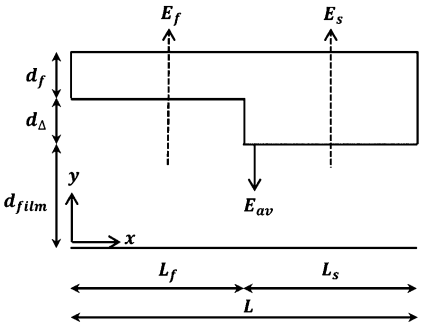


**Fig. 2** One-half wavelength of the periodically varying template and film of suspended nanoparticles.

(Fig. 2). Subscripts s and f refer to slow and fast evaporation regions respectively, and $\Phi_0$ to the initial particle volume fraction in the suspension. The evaporation rates are given by‡

$$E_f = \frac{8.85 \times 10^{-13}}{d_f}\ m\ s^{-1},\ E_s = \frac{8.85 \times 10^{-13}}{d_f + d_\Delta}\ m\ s^{-1} \quad (1)$$

and the average evaporation rate

$$E_{av} = \frac{E_f L_f + E_s L_s}{L_f + L_s}, \quad (2)$$

which is also the speed of descent of the membrane.

Edge effects are ignored and the membrane is taken to be rigid. Scaling vertical distances by $d_\Delta + d_{film}$, horizontal distances by $L$, vertical velocities $v$ by the average evaporation rate $E_{av}$, horizontal velocities $u$ by $E_{av}L/(d_\Delta + d_{film})$ (from continuity) and time $t$ by $(d_\Delta + d_{film})/E_{av}$, the dimensionless convection–diffusion equation for particle volume fraction $\Phi$ is given by

$$Pe\left(\frac{\partial \varphi}{\partial t} + u\frac{\partial \varphi}{\partial x} + v\frac{\partial \varphi}{\partial y}\right) = \frac{\partial}{\partial x}\left[D\frac{\partial \varphi}{\partial x}\right] + \frac{1}{A^2}\frac{\partial}{\partial y}\left[D\frac{\partial \varphi}{\partial y}\right], \quad (3)$$

where $Pe \equiv E_{av}L^2/D_0(d_\Delta + d_{film})$ is a Peclet number with $D_0$ and $D$ being the diffusivity of an isolated sphere and suspension diffusivity, respectively. The Peclet number dictates the importance of convection relative to diffusion in determining particle segregation between regions of fast and slow evaporation. $A \equiv (d_\Delta + d_{film})/L$ is an aspect ratio.

Fluid flow is described by momentum and material conservation, while diffusivity and viscosity are coupled to volume fraction through constitutive relationships. These along with the appropriate boundary conditions are described in the Appendix.

### Independent variables

Four independent variables allow us to affect the dimensions of the deposit and the drying time: two membrane thicknesses along with the initial thickness and concentration of the suspension film. Accessible ranges for these were taken to be $10\ nm \le d_f \le 1\ mm$, $0 \le d_\Delta \le 2d_f$, $100\ nm \le d_{film} \le 1\ mm$, $0.001 \le \Phi_0 \le 0.2$. Particle diameter $a$ was set at 10 nm and ambient temperature was assumed.

† See the Appendix for details.

‡ See the Appendix for estimation of the pervaporation rate.

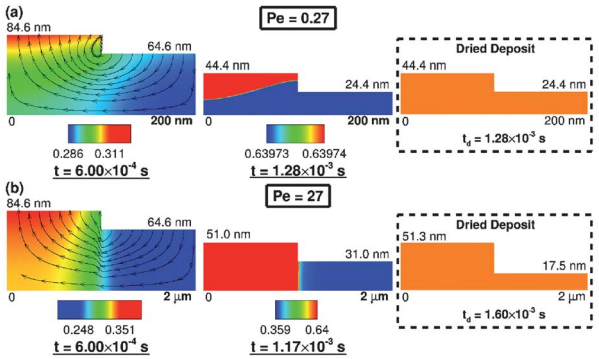


**Fig. 3** Evolution of particulate volume fraction contours and velocity streamlines for (a) 100 nm and (b) 1 μm wide features. The insets on the right show the final dimensions of the dried deposit in each case. The horizontal scale in (b) has been compressed. In both (a) and (b), $d_f = 10$ nm, $d_\Delta = 2d_f$, $d_{film} = 100$ nm, $\Phi_0 = 0.20$ and 10 nm particle diameter.



### Flow and concentration profiles

Fig. 3 shows simulation results for two different feature widths, giving different Peclet numbers. Heterogeneous evaporation induces flow from slow to fast evaporation regions, depicted by the streamlines. For 100 nm wide features, *Pe* is low; diffusion dominates and the suspension dries to uniform random close-packing (RCP) throughout. For 1 μm wide features on the other hand, *Pe* is high ($Pe \propto L^2$); convection dominates, and instead of the entire suspension drying uniformly, the fast evaporation region attains RCP while the slow evaporation region is still fluid. The insets show the final size of the dried deposit; this is the same as shown in the numerical solution for $Pe = 0.27$, whereas at $Pe = 27$, the final deposit is realized once the *entire* suspension has dried. In the latter case, the deposit size is calculated assuming that once the fast evaporation region dries, membrane descent ceases and there is no further transfer of particles from the slow to the fast evaporation region.

It is noteworthy that the simulated deposit dimensions and drying times in these two cases correspond to the diffusive and convective limits (derived later) respectively. These limiting cases are independent of the absolute feature width (they depend only on the relative width $L_f/L_s$). Narrow features (with their small Peclet numbers) tend towards the diffusive limit, whereas broad ones tend towards the convective.

## Bounds on deposit dimensions and drying time

Diffusion dominant and convection dominant limits ($Pe \to 0$ and $Pe \to \infty$ respectively) constitute bounds within which the true particle concentration profile lies. Particle volume fractions averaged over the fast and slow evaporation regions ($\Phi_f(t)$, $\Phi_s(t)$) within these limits follow simply from material balances. These then yield limiting values for the feature and residual layer heights as well as drying time ($t_d$), the quantities of primary interest in the context of such a patterning process. This analysis is outlined below and the solutions summarized in Table 1.

### Diffusive limit ($Pe \to 0$)

In the infinite diffusion limit particle concentration is spatially uniform:

$$\varphi(t) = \left[\frac{\frac{d_\Delta}{d_{film}} + \left(1 + \frac{L_s}{L_f}\right)}{\frac{d_\Delta}{d_{film}} + \left(1 + \frac{L_s}{L_f}\right)\left(1 - \frac{E_{av}t}{d_{film}}\right)}\right]\varphi_0. \quad (4)$$

As evaporation proceeds, the membrane continues to descend until it comes into contact with either uniformly random close-packed particles or undried monolayers in the slow evaporation regions. In a given system, the former happens if $\varphi(t = (d_{film} - a)/E_{av}) \geq 0.64$ and the latter otherwise. We refer to the time at which the membrane ceases to descend as $t_m$ and the total time it takes for the entire suspension to dry as the drying time $t_d$.

For systems in which uniform random close packing (RCP) is the operating regime, the drying time ($t_d = t_m$) follows simply by setting $\Phi(t) = 0.64$ in eqn (4). Deposit heights are then given by $h_{rl} = d_{film} - E_{av}t_m$ and $h_{ft} = h_{rl} + d_\Delta$. For a monolayer residual layer on the other hand, the drying time is the time it takes for the membrane to reach a point where it is one particle diameter away from the substrate plus the additional time for the fast evaporation region to dry, while the feature height is given by $h_{ft} = (d_\Delta + a)\Phi(t_m)/0.64$.

### Convective limit ($Pe \to \infty$)

Now we consider a situation such that there is no diffusion parallel to the substrate. In the slow evaporation region, the volume of liquid:

$$l_s = -L_s(d_{film} - E_{av}t)(1 - \varphi_s), \quad (5)$$

$$\Rightarrow \frac{dl_s}{dt} = -L_s\left(d_{film} - E_{av}t\right)\frac{d\varphi_s}{dt} - L_sE_{av}(1 - \varphi_s). \quad (6)$$

Incompressibility dictates that the rate of convection between the slow and fast evaporation regions is $(E_{av} - E_s)L_s$. The rate of change of liquid volume in the slow evaporation region is therefore given by

$$\frac{dl_s}{dt} = -L_s[E_s + (1 - \varphi_s)(E_{av} - E_s)]. \quad (7)$$

Comparing eqn (6) and (7) gives:

$$\varphi_s(t) = \frac{\varphi_0}{\left(1 - \frac{E_{av}t}{d_{film}}\right)^{E_s/E_{av}}}. \quad (8)$$

The volume fraction of particles averaged over the fast evaporation region then follows from conservation of particles:

$$\varphi_f(t) = \left[\frac{\frac{d_\Delta}{d_{film}} + \left(1 + \frac{L_s}{L_f}\right) - \frac{L_s}{L_f}\left(1 - \frac{E_{av}t}{d_{film}}\right)^{1-(E_s/E_{av})}}{\frac{d_\Delta}{d_{film}} + 1 - \frac{E_{av}t}{d_{film}}}\right]\varphi_0. \quad (9)$$

Eqn (8) and (9) are valid as long as the membrane continues to descend. It ceases to descend when it comes into

**Table 1** Analytically derived bounds on deposit heights and drying time[a]

| | Diffusive limit ($Pe \to 0$) | Convective limit ($Pe \to \infty$) |
|---|---|---|
| Regime | Uniform RCP | RCP in fast evaporation region |
| Operative when: | $\varphi\left(t=\frac{d_{film}-a}{E_{av}}\right) \geq 0.64$ | $\varphi_f(t\|\varphi_s=0.64) > 0.64$ *and* $t\|(\varphi_f=0.64) < (d_{film}-a)/E_{av}$ |
| $t_m$ | $t_d$ | Given by polynomial eq. below[a] |
| $h_{ft}$ | $h_{rl}+d_\Delta$ | $d_\Delta + d_{film} - E_{av}t_m$ |
| $h_{rl}$ | $d_{film}\left(\frac{\varphi_0}{0.64}\right) - \frac{d_\Delta}{1+L_s/L_f}\left(1-\frac{\varphi_0}{0.64}\right)$ | $\frac{\varphi_s(t_m)}{0.64}(d_{film}-E_{av}t_m)$ |
| $t_d$ | $\frac{1}{E_{av}}\left(d_{film}+\frac{d_\Delta}{1+L_s/L_f}\right)\left(1-\frac{\varphi_0}{0.64}\right)$ | $t_m+\frac{1}{E_s}\left(1-\frac{\varphi_s(t_m)}{0.64}\right)\left(d_{film}-E_{av}t_m\right)$ |

| | RCP in slow evaporation region |
|---|---|
| Operative when: | $\varphi_f(t\|\varphi_s=0.64) < 0.64$ *and* $t\|(\varphi_f=0.64) < (d_{film}-a)/E_{av}$ |
| $t_m$ | $\frac{d_{film}}{E_{av}}\left[1-\left(\frac{\varphi_0}{0.64}\right)^{E_{av}/E_s}\right]$ |
| $h_{ft}$ | $\frac{\varphi_f(t_m)}{0.64}\left[d_\Delta + d_{film}\left(\frac{\varphi_0}{0.64}\right)^{E_{av}/E_s}\right]$ |
| $h_{rl}$ | $d_{film}\left(\frac{\varphi_0}{0.64}\right)^{E_{av}/E_s}$ |
| $t_d$ | $t_m+\frac{1}{E_f}\left(1-\frac{\varphi_f(t_m)}{0.64}\right)\left[d_\Delta + d_{film}\left(\frac{\varphi_0}{0.64}\right)^{E_{av}/E_s}\right]$ |

| | Monolayer $h_{rl}$ | Monolayer $h_{rl}$ |
|---|---|---|
| Regime | | |
| Operative when: | $\varphi\left(t=\frac{d_{film}-a}{E_{av}}\right) < 0.64$ | $\varphi_f(t_m) < 0.64$ *and* $\varphi_s(t_m) < 0.64$ |
| $t_m$ | $(d_{film}-a)/E_{av}$ | $(d_{film}-a)/E_{av}$ |
| $h_{ft}$ | $[\varphi(t_m)/0.64](d_\Delta + a)$ | $[\varphi_f(t_m)/0.64](d_\Delta + a)$ |
| $h_{rl}$ | $a$ | $a$ |
| $t_d$ | $t_m+\frac{1}{E_f}\left(1-\frac{\varphi(t_m)}{0.64}\right)(d_\Delta + a)$ | $t_m+\frac{1}{E_f}\left(1-\frac{\varphi_f(t_m)}{0.64}\right)(d_\Delta + a)$ |

[a] $\frac{L_s}{L_f}\left(1-\frac{E_{av}t_m}{d_{film}}\right)^{1-E_s/E_{av}}\left(\frac{\varphi_0}{0.64}\right) - \left(1+\frac{L_s}{L_f}\right)\frac{\varphi_0}{0.64} + \left(1-\frac{\varphi_0}{0.64}\right)\frac{d_\Delta}{d_{film}} - \frac{E_{av}t_m}{d_{film}} + 1 = 0.$

contact with random close packed particles in either the slow or the fast evaporation regions, or with undried monolayers in the slow evaporation regions. The operative regime within these three possibilities can be inferred by using eqn (8) and (9) to determine whether either the slow or the fast evaporation regions attain random close packing before the membrane reaches a distance of one particle diameter from the substrate.

For systems in which the fast evaporation regions are the first to dry, the time at which the membrane stops descending ($t_m$) is given by setting $\Phi_f(t) = 0.64$ in eqn (9) and solving the resulting polynomial numerically. Deposit heights are then given by $h_{ft} = d_\Delta + d_{film} - E_{av}t_m$ and $h_{rl} = (d_{film} - E_{av}t_m)\Phi_s(t_m)/0.64$. When the slow evaporation regions dry first, $t_m$ is simply obtainable by setting $\Phi_s(t_m) = 0.64$ in (8), while $h_{ft} = (d_\Delta + d_{film} - E_{av}t_m)\Phi_f(t_m)/0.64$ and $h_{rl} = d_{film} - E_{av}t_m$. Finally, when the monolayer $h_{rl}$ regime is operative, the drying time is the time it takes for the membrane to reach a point where it is one particle diameter away from the substrate plus the additional time it takes for the fast evaporation regions to dry, while $h_{ft} = (d_\Delta + a)\Phi_f(t_m)/0.64$.

The results of the analysis are summarized in the Table 1, which should be used in conjunction with eqn (4), (8) and (9) for $\Phi(t)$, $\Phi_s(t)$ and $\Phi_f(t)$ respectively to arrive at limiting values for the deposit heights and drying time. These serve as a heuristic to guide experiments targeting specific feature and residual layer dimensions as well as drying times.

## Effect of independent variables

We now investigate the role played by each of the independent variables in determining the dimensions of the deposit and the drying time required to achieve it. The primary dependent process variables are the differential feature height ($h_{ft} - h_{rl}$),

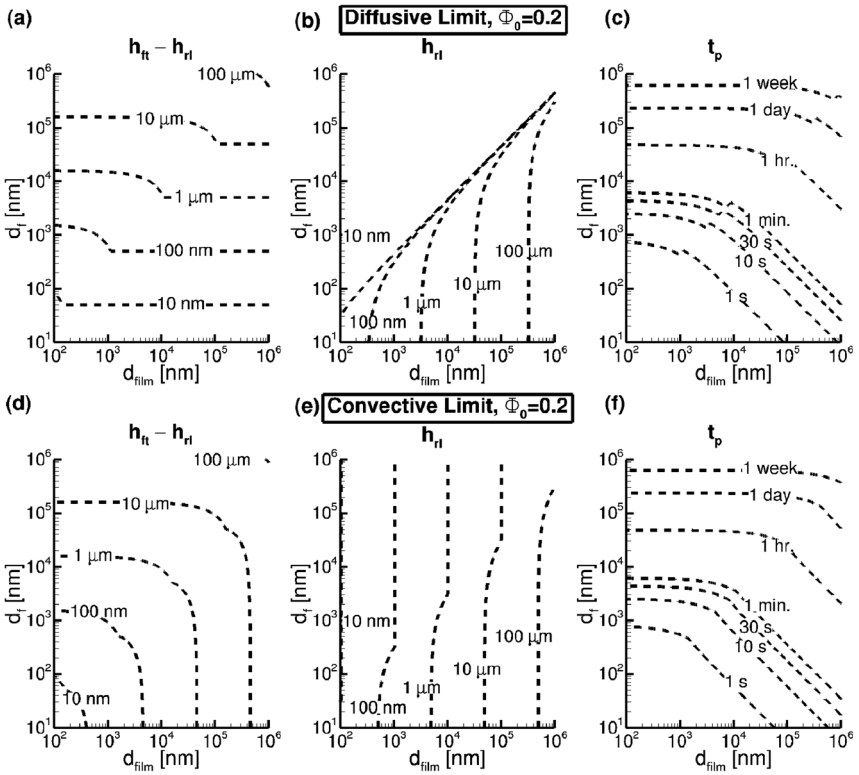


**Fig. 4** (a) and (d) Differential feature height (b) and (e) residual layer height and (c) and (f) drying time as a function of film height and template thickness in the (a)–(c) diffusive and (d)–(f) convective limits, with $d_\Delta = 2d_f$, $\Phi_0 = 0.2$, $L_f/L_s = 1$ and 10 nm diameter particles.

residual layer thickness ($h_{rl}$) and the drying time ($t_d$). Fig. 4 shows how these quantities vary with membrane thickness ($d_f$) and initial suspension film height ($d_{film}$) within the diffusive and convective limits, with $d_\Delta = 2d_f$. Note that increasing $d_f$ has two opposing effects: it reduces *Pe*, thus hampering particle segregation by pushing the system towards the diffusive limit, but allows larger $d_\Delta$, thus increasing the volume of the fast evaporation region and resultantly the height of the feature within the diffusive limit.

It is evident in Fig. 4 that thick membranes result in more pronounced features as well as thinner residual layers at the cost of longer drying times. As $d_f$ increases, so does the volume of the fast evaporation region (since $d_\Delta = 2d_f$), producing higher features. Thick suspension films also produce higher features with longer drying times, but also thicker residual layers. This is expected, since at a constant initial volume fraction of particles, thick suspension films have more particles as well as more fluid that needs to evaporate.

Discontinuities in contour lines represent transition to a different operating regime, with two different regimes being operative in different regions of the parameter space. In the diffusive limit, undried monolayers impede membrane descent at high $d_f$ and/or low $d_{film}$ (top left of the plots in Fig. 4(a–c)) due to the large difference in volume between the two regions. The residual layer height (Fig. 4(b)) is therefore one particle diameter, and the drying time (Fig. 4(c)) is relatively insensitive to film height since the total volume of the suspension is determined mainly by $d_f$ through $d_\Delta$. At low $d_f$ and/or high $d_{film}$ (bottom right of the plots in Fig. 4(a–c)), on the other hand, uniform RCP occurs when the membrane is more than one particle diameter away from the substrate. In this domain, the residual layer and feature heights increase equally with $d_{film}$, leaving the differential height (Fig. 4(a)) unchanged. The drying time (Fig. 4(c)) becomes a function of both $d_f$ and $d_{film}$.

In the convective limit, the slow evaporation region dries first at high $d_f$ and/or low $d_{film}$ (top left of the plots in Fig. 4(d–f)) due to its smaller volume. The height of the residual layer in this part of the parameter space is unaffected by $d_f$ since the membrane–substrate distance at which the slow evaporation region attains RCP is insensitive to $d_f$. The differential feature height and drying time do however depend on $d_f$. At low $d_f$ and/or high $d_{film}$ (bottom right of the plots in Fig. 4(d–f)), the fast evaporation region dries first, and drying time as well as deposit heights vary with both $d_f$ and $d_{film}$.

Thus, thick films drying under thick templates result in the most pronounced features but also long drying times. The diffusive and convective limits predict similar values for these quantities, except for the feature height for thick films dried under thin templates and the residual layer height for thin films dried under thick templates. Interestingly, in the latter case, the diffusive limit predicts a thinner residual layer than the convective. This is because in these cases particle concentration in the slow evaporation region within the convective limit increases at a faster rate than the fast evaporation region due to its much smaller volume. There exists a small region of the parameter space wherein residual layer height is very sensitive to suspension film and template thicknesses (Fig. 4(b)), possibly leading to experimental uncertainty. Differential feature heights

 

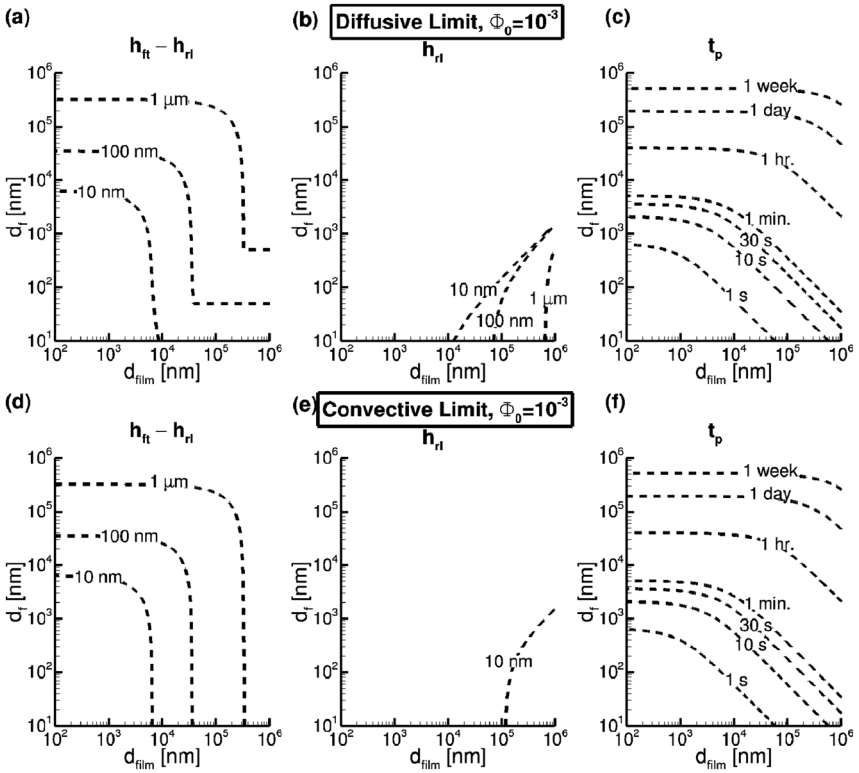


**Fig. 5** (a) and (d) Differential feature height (b) and (e) residual layer height and (c) and (f) drying time as a function of film height and template thickness in the (a)–(c) diffusive and (d)–(f) convective limits, with $d_\Delta = 2d_f$, $\Phi_0 = 10^{-3}$, $L_f/L_s = 1$ and 10 nm diameter particles.

of hundreds of nanometers can be achieved with a drying time of less than 30 s.

Fig. 5 depicts results at a lower initial volume fraction of particles. The general trends in deposit dimensions with varying film height and template thickness remain largely unchanged but are shifted to smaller deposit sizes due to the presence of fewer particles. The operative regimes for dilute suspensions are the same as for relatively concentrated ones except that at high $d_f$ and/or low $d_{film}$ within the convective limit (top left of the plots in Fig. 5) undried monolayers instead of RCP in the slow evaporation region impede membrane descent. As a result, at a low initial concentration of particles (Fig. 5(b and e)), there exists a large parameter space wherein a monolayered residual layer is predicted by both limiting cases. Such a region is barely extant at higher particle concentrations (Fig. 4(b and e)). Low concentrations are therefore preferable if thin residual layers are of importance. This is relevant when isolated features are desired instead of contiguous films, in which case a film with a monolayered residual layer could be deposited and the residual layer possibly sonicated away prior to sintering.[54]

Two further controls on the process are temperature and particle size. Evaporation rate has been shown to increase exponentially with temperature,[55–57] while the rate of diffusion only increases linearly (see eqn (A8)). As a result, the Peclet number is expected to increase with temperature, making more pronounced features patternable with faster drying times. Particle size sets the minimum residual layer height, and *Pe* is proportional to it (through diffusivity). Therefore, the largest feasible particles for a mechanically stable deposit of the desired size are best used to maximize *Pe* for efficient particle segregation.

Next we investigate how templated evaporative lithography compares with free surface evaporation[44] in depositing features of various widths. Fig. 6 shows the differential feature heights

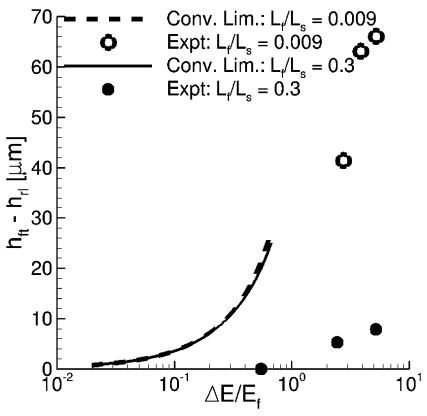


**Fig. 6** Differential feature height as a function of the dimensionless difference between the fast and slow evaporation rates at two different relative feature widths with a *micro*particle suspension. Shown is the relevant limit for templated evaporative lithography (lines; $d_f$ = 100 nm and $d_\Delta = 0$–$2d_f$) and experimental results reported[44] for free surface evaporation (points) with $d_{film}$ = 100 μm, $\Phi_0$ = 0.30 and 1.18 μm diameter particles. The drying time is approximately 10 seconds for templated lithography and 2 hours for free surface evaporation.

resulting from a *micro*particle suspension within the two techniques, with the *x*-axis depicting how much the fast and slow evaporation rates differ. Only the convective limit is shown for templated evaporation since the Peclet number ranges from $4 \times 10^5$ to $4 \times 10^8$ for this system. These curves do not extend to higher evaporation rate differences due to limits on membrane fabrication ($d_\Delta \leq 2d_f$). The drying times for the deposits shown are approximately 10 seconds for templated evaporative lithography and 2 hours for free surface evaporation. Therefore, templated evaporative lithography is able to produce features of half the size as free surface evaporation within a drying time which is two orders of magnitude smaller.

In free surface evaporation, the difference between the two evaporation rates (and hence the attainable differential feature height) is a function of the width of features relative to the distance between them, with narrower features ($L_f/L_s = 0.009$) being several times higher than broader ones ($L_f/L_s = 0.3$). Moreover, the two evaporation rates, and hence also the feature and residual layer height, are coupled and cannot be controlled individually. In templated lithography, on the other hand, feature height can be seen in Fig. 6 to be insensitive to relative feature width. Also, both evaporation rates can be controlled individually *via* membrane thicknesses ($d_f$ and $d_\Delta$), providing independent control over feature and residual layer height. When nanoscaled deposits are desired, the constraint which free surface evaporation imposes in terms of a maximum relative feature width above which features are not formed is likely to be considerably more severe (and possibly even prohibitive) due to stronger diffusion.

### Performance limits

One further aspect of interest is the best performance, taken here to be defined by short drying times and thin residual layers, achievable within such a system and how it is influenced by desired feature size. In order to investigate this we approximated the differential height and drying time for any given system to be the average of their values within the diffusive and convective limits,§ and optimized the independent variables to achieve the minimum drying time or residual layer height. Fig. 7(a) shows the minimum attainable drying time and associated residual layer height for a range of differential feature heights. Both can be seen to increase linearly, and the minimum time is approximately 1 s per 10 μm of differential feature height:

$$\min t_d[\mathrm{s}] \approx 1.3 \times 10^{-4} \times (h_{ft} - h_{rl})[\mathrm{nm}] \quad (10)$$

$$h_{rl}(\min t_d) \approx 2.4 \times (h_{ft} - h_{rl}) - 13 \quad (11)$$

These drying times represent the ideal limit, since they are dependent on 10 nm thick templates which are difficult to realize. Even with a more usual membrane thickness of 1 μm, however, the minimum time would be ten seconds per micron of feature height above the residual layer, which is acceptable for high throughput processing.

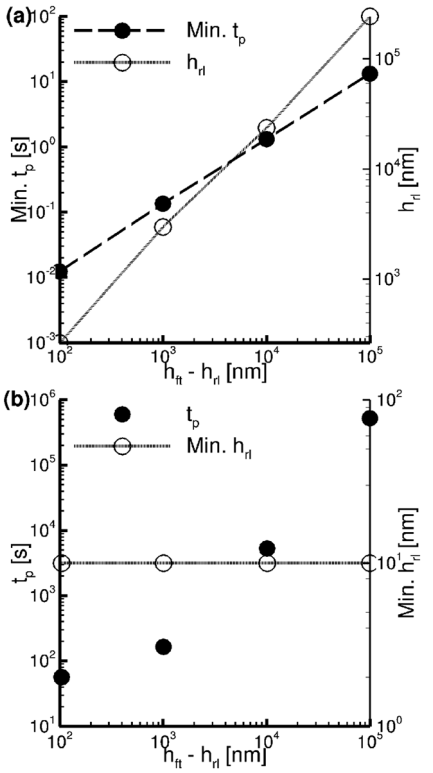


**Fig. 7** Minimum attainable drying time and resulting residual layer height (a) and minimum attainable residual layer height and resulting drying time (b) as a function of differential feature height, for deposits with $L_f/L_s = 1$ and 10 nm diameter particles (at $h_{ft} - h_{rl} = 10^2$, $10^3$, $10^4$, $10^5$ nm, the values of the independent variables are: $d_f = 10$ nm, $d_\Delta = 12$, 12, 20, 18 nm, $d_{film} = 1$, 11, 92, 940 μm, $\Phi_0 = 0.2$ in (a), while in (b), $d_f = 10$, 10, 50, 500 μm, $d_\Delta = 3.9$, 14, 100, 1000 μm, $d_{film} = 1$ μm, $\Phi_0 = 1.31 \times 10^{-2}$, $4.12 \times 10^{-2}$, $6.33 \times 10^{-2}$, $6.33 \times 10^{-2}$).

Another performance criterion is residual layer height, the lower limit on which is one particle diameter (as mentioned previously, this is especially relevant when isolated features are desired). Fig. 7(b) depicts the minimum drying time for a range of feature heights with monolayered residual layers. It can be seen that the drying time increases at an accelerating rate with the desired feature height, and that it exceeds the minimum drying time (without the monolayer residual layer constraint) by as much as approximately four orders of magnitude in seconds. Isolated features up to a micron high, however, can be deposited within around 200 seconds. Interestingly, given enough time, even millimeter sized features are patternable with 10 nm diameter monolayered residual layers.

## Conclusions

Spatially heterogeneous evaporation caused by a templated membrane drives an accumulation of particles in regions with fast evaporation, resulting in a deposit with raised features. Importantly, evaporation is rapid enough for continuous

§ As seen earlier, for certain systems differential feature heights predicted by the diffusive and convective limits differ by orders of magnitude, and so this serves only as a coarse estimate. However, this is mitigated by the fact that none of the estimated optimal systems lie within that region of the parameter space.

processing to be feasible, and nanosized deposits are achievable. Films with 10 nm to 100 μm sized features can be patterned with a drying time of 1–100 seconds per 10 μm of differential feature height, depending upon the thickness of the membrane template. Experiments targeting specific deposits can be guided by analytically derived bounds on deposit dimensions and drying time (and optionally also by simulation). The analysis here shows that templated evaporative lithography presents potential improvement over free surface evaporation by making nanosized deposits attainable, reducing the drying time by two orders of magnitude, depositing sharply defined patterns and allowing independent control over each of their dimensions. It constitutes a promising route for the low-cost deposition of three-dimensional metallic nanostructures of varying shapes over large areas in high-throughput processing.

## Appendix

### Estimating the evaporation rate

The drying time for pattern deposition, critical to the viability of any technique as a practical industrial process, is governed in this case by the pervaporation rate of the liquid. Neglecting evaporative cooling, the evaporation rate can be estimated from data for gas permeation in membranes (the liquid being equivalent to a gas at a partial pressure equal to the vapor pressure of the liquid):

$$J = P \times \frac{\Delta p}{d}. \tag{A1}$$

here $J$ is the evaporative flux, $P$ the permeability of the membrane (usually expressed in Barriers $\equiv 10^{-10}$ cm$^3$ (STP) cm/(cm$^2$ s cmHg)), $\Delta p$ the partial pressure driving force and $d$ the membrane thickness. Considering a toluene solvent at 20 °C covered by a PDMS membrane with 33% silica:[58]

$$P = 9130\text{Barriers} = \frac{4.03}{10^{13}}\frac{\text{m}}{\text{s}}\frac{\text{m}}{\text{cmHg}}. \tag{A2}$$

The unit conversion is done so that eqn (A1) yields an evaporation rate in m s$^{-1}$ (*i.e.* the rate of reduction of film thickness). When a sweep gas is used (so that partial pressure of solvent at the unpatterned face of the membrane is zero), this gives:

$$E = \frac{8.85 \times 10^{-13}}{d}\,\text{m s}^{-1} \tag{A3}$$

*i.e.* a 10 nm thick membrane results in an evaporation rate of 88.5 μm s$^{-1}$. This is comparable to pervaporation, wherein rates in excess of 100 μm s$^{-1}$ have been reported.[59–61] Harris *et al.*[44] reported free-surface drying rates of ≈0.014 μm s$^{-1}$. Hence the membrane, by its imposition of a steep chemical potential gradient, has a dramatic effect on drying time, dealing with an important barrier to industrial application of this bottom-up technique.

### Evaluating the numerical solution

Diffusivity $D$ is given by the Stokes–Einstein equation:[62]

$$D(\varphi) = K(\varphi)\frac{d}{d\varphi}[\varphi Z(\varphi)] \tag{A4}$$

where $K$ is the particle sedimentation coefficient and $Z$ the compressibility factor, which account for hydrodynamic and thermodynamic interactions respectively. These, along with the dimensionless viscosity of the dispersion $\mu$ and the isolated sphere diffusivity $D_0$, are taken to be:[62]

$$K(\varphi) = (1 - \varphi)^{6.55}, \tag{A5}$$

$$Z(\varphi) = \frac{1.85}{0.64 - \varphi}, \tag{A6}$$

$$\mu = \left(1 - \frac{\varphi}{0.64}\right)^{-2}, \tag{A7}$$

$$D_0 = \frac{k_B T}{3\pi\mu_0 a}, \tag{A8}$$

with particle diameter $a$, liquid viscosity $\mu_0$, temperature $T$ and Boltzmann constant $k_B$.

Fluid flow is described by momentum and material conservation. Ignoring gravitational effects and taking the fluid to be Newtonian, these are:

$$Re\left(\frac{\partial u}{\partial t} + u\frac{\partial u}{\partial x} + v\frac{\partial u}{\partial y}\right) = -\frac{\partial p}{\partial x} + A\frac{\partial}{\partial x}\left[2\mu\frac{\partial u}{\partial x}\right] + \frac{1}{A}\frac{\partial}{\partial y}\left[\mu\frac{\partial u}{\partial y}\right] + A\frac{\partial}{\partial y}\left[\mu\frac{\partial v}{\partial x}\right] \tag{A9}$$

$$Re\left(\frac{\partial v}{\partial t} + u\frac{\partial v}{\partial x} + v\frac{\partial v}{\partial y}\right) = -\frac{1}{A^2}\frac{\partial p}{\partial y} + \frac{1}{A}\frac{\partial}{\partial x}\left[\mu\frac{\partial u}{\partial y}\right] + A\frac{\partial}{\partial x}\left[\mu\frac{\partial v}{\partial x}\right] + \frac{1}{A}\frac{\partial}{\partial y}\left[2\mu\frac{\partial v}{\partial y}\right] \tag{A10}$$

$$\frac{\partial u}{\partial x} + \frac{\partial v}{\partial y} = 0 \tag{A11}$$

with the variables being in dimensionless form. Here pressure $p$, which includes the osmotic pressure, is scaled by $\mu_0 E_{av} L/(d_\Delta + d_{film})^2$ and the Reynolds number $Re$ is defined as $\rho E_{av} L/\mu_0$. Boundary conditions for eqn (3) are no penetration at all boundaries, which reduces to

$$\frac{1}{A^2 Pe} D\frac{\partial \varphi}{\partial y} - v\varphi = \varphi \tag{A12}$$

at the horizontal faces of the membrane and

$$\boldsymbol{n}\cdot\nabla\varphi = 0 \tag{A13}$$

at all other boundaries, with $\boldsymbol{n}$ being a unit normal at the relevant boundary. For eqn (A9) and (A10), symmetry boundary conditions prevail at the fluid boundaries of the domain. No slip is assumed at the vertical face of the membrane (as well as at the substrate), while at its horizontal faces, the $y$-velocities are $E_s/E_{av} - 1$ and $E_f/E_{av} - 1$ in the slow and fast evaporation regions respectively. A Dirichlet point constraint for pressure was imposed at the top right corner of the slow evaporation region (Fig. 2). Since the flow is driven by the velocity boundary conditions at the template due to evaporation, we may solve for

this net pressure without breaking the pressure into its osmotic and fluid components.

The aforementioned system of equations was solved using COMSOL Multiphysics 3.5a. Membrane descent was modeled with the Automatic Lagrangian-Eulerian (ALE) mode with remeshing enabled. A PARDISO direct solver was used in conjunction with BDF time stepping while all other settings were the COMSOL default values. Meshes with less than 10 000 quadratic Lagrange elements, with a boundary layer at the membrane when needed, were found to be sufficient for convergence.



## Acknowledgements

The authors thank Drs S. V. Sreenivasan and Shrawan Singhal for their helpful comments on this work. The authors also gratefully acknowledge support from NSF Scalable Nano-Manufacturing grant # 1120823.

## References

1 S. Linic, P. Christopher and D. B. Ingram, *Nat. Mater.*, 2011, **10**, 911–921.
2 J. A. Schuller, E. S. Barnard, W. Cai, Y. C. Jun, J. S. White and M. L. Brongersma, *Nat. Mater.*, 2010, **9**, 193–204.
3 F. J. Himpsel, J. E. Ortega, G. J. Mankey and R. F. Willis, *Adv. Phys.*, 1998, **47**, 511–597.
4 S. Y. Chou, *Proc. IEEE*, 1997, **85**, 652–671.
5 S. Y. Lin, E. Chow, V. Hietala, P. R. Villeneuve and J. D. Joannopoulos, *Science*, 1998, **282**, 274–276.
6 O. Painter, R. K. Lee, A. Scherer, A. Yariv, J. D. O'Brien, P. D. Dapkus and I. Kim, *Science*, 1999, **284**, 1819–1821.
7 Y. Masuda, T. Koumura, T. Okawa and K. Koumoto, *J. Colloid Interface Sci.*, 2003, **263**, 190–195.
8 H. Gau, S. Herminghaus, P. Lenz and R. Lipowsky, *Science*, 1999, **283**, 46–49.
9 A. Hartl, E. Schmich, J. A. Garrido, J. Hernando, S. C. R. Catharino, S. Walter, P. Feulner, A. Kromka, D. Steinmuller and M. Stutzmann, *Nat. Mater.*, 2004, **3**, 736–742.
10 W. Yang, O. Auciello, J. E. Butler, W. Cai, J. A. Carlisle, J. E. Gerbi, D. M. Gruen, T. Knickerbocker, T. L. Lasseter, J. N. Russell, L. M. Smith and R. J. Hamers, *Nat. Mater.*, 2002, **1**, 253–257.
11 C. L. Haynes and R. P. Van Duyne, *J. Phys. Chem. B*, 2001, **105**, 5599–5611.
12 B. Yang, J. H. Zhang, Y. F. Li and X. M. Zhang, *Adv. Mater.*, 2010, **22**, 4249–4269.
13 N. V. Dziomkina and G. J. Vancso, *Soft Matter*, 2005, **1**, 265–279.
14 O. D. Velev and E. W. Kaler, *Langmuir*, 1999, **15**, 3693–3698.
15 S. T. Liu, T. Zhu, R. S. Hu and Z. F. Liu, *Phys. Chem. Chem. Phys.*, 2002, **4**, 6059–6062.
16 R. C. Hayward, D. A. Saville and I. A. Aksay, *Nature*, 2000, **404**, 56–59.
17 J. H. Zhang, X. Zhang, D. F. Zhu, X. A. Li, X. M. Zhang, T. Q. Wang and B. Yang, *Langmuir*, 2010, **26**, 17936–17942.
18 R. D. Deegan, O. Bakajin, T. F. Dupont, G. Huber, S. R. Nagel and T. A. Witten, *Phys. Rev. E: Stat., Nonlinear, Soft Matter Phys.*, 2000, **62**, 756–765.
19 H. Hu and R. G. Larson, *J. Phys. Chem. B*, 2002, **106**, 1334–1344.
20 R. D. Deegan, O. Bakajin, T. F. Dupont, G. Huber, S. R. Nagel and T. A. Witten, *Nature*, 1997, **389**, 827–829.
21 P. J. Yunker, T. Still, M. A. Lohr and A. G. Yodh, *Nature*, 2011, **476**, 308–311.
22 Y. O. Popov, *Phys. Rev. E: Stat.,Nonlinear, Soft Matter Phys.*, 2005, **71**, 036313.
23 E. Rabani, D. R. Reichman, P. L. Geissler and L. E. Brus, *Nature*, 2003, **426**, 271–274.
24 S. G. Yiantsios and B. G. Higgins, *Phys. Fluids*, 2006, **18**, 082103.
25 A. F. Routh and W. B. Zimmerman, *Chem. Eng. Sci.*, 2004, **59**, 2961–2968.
26 A. F. Routh and W. B. Russel, *AIChE J.*, 1998, **44**, 2088–2098.
27 U. Thiele, I. Vancea, A. J. Archer, M. J. Robbins, L. Frastia, A. Stannard, E. Pauliac-Vaujour, C. P. Martin, M. O. Blunt and P. J. Moriarty, *J. Phys.: Condens. Matter*, 2009, **21**, 264016.
28 F. Jarai-Szabo, S. Astilean and Z. Neda, *Chem. Phys. Lett.*, 2005, **408**, 241–246.
29 M. Fujita and Y. Yamaguchi, *Int. Polym. Process.*, 2007, **22**, 16–21.
30 J. Xu, J. Xia, S. W. Hong, Z. Lin, F. Qiu and Y. Yang, *Phys. Rev. Lett.*, 2006, **96**, 066104.
31 J. Xu, J. Xia and Z. Lin, *Angew. Chem., Int. Ed.*, 2007, **46**, 1860–1863.
32 H. S. Kim, C. H. Lee, P. K. Sudeep, T. Emrick and A. J. Crosby, *Adv. Mater.*, 2010, **22**, 4600–4604.
33 A. Stannard, *J. Phys.: Condens. Matter*, 2011, **23**, 083001.
34 W. Han and Z. Lin, *Angew. Chem., Int. Ed.*, 2012, **51**, 1534–1546.
35 R. G. Larson, *Angew. Chem., Int. Ed.*, 2012, **51**, 2546–2548.
36 S. Choi, A. Jamshidi, T. J. Seok, M. C. Wu, T. I. Zohdi and A. P. Pisano, *Langmuir*, 2012, **28**, 3102–3111.
37 X. Tang, S. J. O'Shea and I. U. Vakarelski, *Adv. Mater.*, 2010, **22**, 5150–5153.
38 A. Georgiadis, A. F. Routh, M. W. Murray and J. L. Keddie, *Soft Matter*, 2011, **7**, 11098–11102.
39 W. Han, M. Byun and Z. Lin, *J. Mater. Chem.*, 2011, **21**, 16968–16972.
40 P. Kumnorkaew, Y. K. Ee, N. Tansu and J. F. Gilchrist, *Langmuir*, 2008, **24**, 12150–12157.
41 Z. L. Wang, R. R. Bao, X. J. Zhang, X. M. Ou, C. S. Lee, J. C. Chang and X. H. Zhang, *Angew. Chem., Int. Ed.*, 2011, **50**, 2811–2815.
42 J. A. Lewis, D. J. Harris and J. C. Conrad, *Philos. Trans. R. Soc. London, Ser. A*, 2009, **367**, 5157–5165.
43 D. J. Harris and J. A. Lewis, *Langmuir*, 2008, **24**, 3681–3685.
44 D. J. Harris, H. Hu, J. C. Conrad and J. A. Lewis, *Phys. Rev. Lett.*, 2007, **98**, 148301.
45 Z. Q. Lin, S. W. Hong and M. Byun, *Angew. Chem., Int. Ed.*, 2009, **48**, 512–516.
46 C. J. Brinker, Y. F. Lu, A. Sellinger and H. Y. Fan, *Adv. Mater.*, 1999, **11**, 579.

 

47 S. Maenosono, T. Okubo and Y. Yamaguchi, *J. Nanopart. Res.*, 2003, **5**, 5–15.
48 X. Zhang, X. Wang, W. Kong, G. Yi and J. Jia, *Appl. Surf. Sci.*, 2011, **258**, 113–119.
49 J. Li, M. Wang and Y. Shen, *Surf. Coat. Technol.*, 2012, **206**, 2161–2167.
50 E. K. F. Yim, R. M. Reano, S. W. Pang, A. F. Yee, C. S. Chen and K. W. Leong, *Biomaterials*, 2005, **26**, 5405–5413.
51 H. J. Nam, J.-H. Kim, D.-Y. Jung, J. B. Park and H. S. Lee, *Appl. Surf. Sci.*, 2008, **254**, 5134–5140.
52 L. Wang, Y. Ding, B. Lu and Z. Qiu, *Novel Nano-scale Overlay Alignment Method for Room-temperature Imprint Lithography*, 2006.
53 N. Li, W. Wu and S. Y. Chou, *Nano Lett.*, 2006, **6**, 2626–2629.
54 C. L. Haynes and R. P. Van Duyne, *J. Phys. Chem. B*, 2001, **105**, 5599–5611.
55 F. Xiangli, Y. Chen, W. Jin and N. Xu, *Ind. Eng. Chem. Res.*, 2007, **46**, 2224–2230.
56 H. Wu, L. Liu, F. Pan, C. Hu and Z. Jiang, *Sep. Purif. Technol.*, 2006, **51**, 352–358.
57 S. V. Satyanarayana, A. Sharma and P. K. Bhattacharya, *Chem. Eng. J.*, 2004, **102**, 171–184.
58 J. E. Mark, *Polymer Data Handbook*, Oxford University Press, Oxford, 1999.
59 H. J. Kim, S. S. Nah and B. R. Min, *Adv. Environ. Res.*, 2002, **6**, 255–264.
60 P. Peng, B. Shi and Y. Lan, *Sep. Sci. Technol.*, 2011, **46**, 420–427.
61 X. Zhan, J.-d. Li, J.-q. Huang and C.-x. Chen, *Chin. J. Polym. Sci.*, 2009, **27**, 533–542.
62 W. B. Russel, D. A. Saville and W. R. Schowater, *Colloidal Dispersions*, Cambridge University Press, Cambridge, 1989.